

# $\mathcal{PT}$ -activated non-Hermitian skin modes

Zhoutao Lei,<sup>1</sup> Ching Hua Lee,<sup>2,\*</sup> and Linhu Li<sup>1,†</sup>

<sup>1</sup>*Guangdong Provincial Key Laboratory of Quantum Metrology and Sensing & School of Physics and Astronomy, Sun Yat-Sen University (Zhuhai Campus), Zhuhai 519082, China*

<sup>2</sup>*Department of Physics, National University of Singapore, Singapore 117551, Republic of Singapore*  
(Dated: May 9, 2023)

Parity-time ( $\mathcal{PT}$ ) symmetry is a cornerstone of non-Hermitian physics as it ensures real energies for stable experimental realization of non-Hermitian phenomena. In this work, we propose  $\mathcal{PT}$  symmetry as a paradigm for designing new families of higher-dimensional non-Hermitian states with unique bulk, surface, hinge or corner dynamics. Through systematically breaking or restoring  $\mathcal{PT}$  symmetry in different sectors of a system, we can selectively “activate” or manipulate the non-Hermitian skin effect (NHSE) in both the bulk and topological boundary states. Some fascinating new phenomena include the directional toggling of the NHSE, an intrinsic hybrid skin-topological effect and the flow of boundary states without chiral or dynamical pumping. Our results extend richly into 3D or higher, with more sophisticated interplay with hybrid skin-topological localizations and  $\mathcal{CP}$  symmetry. Based on non-interacting lattices,  $\mathcal{PT}$ -activated NHSE phenomena can be observed in various optical, photonic, electric and quantum platforms that admit gain/loss and non-reciprocity.

*Introduction.*— Parity-time ( $\mathcal{PT}$ ) symmetry is a key ingredient in contemporary non-Hermitian physics [1–3]. As a special type of pseudo-Hermiticity [4],  $\mathcal{PT}$  symmetry guarantees real eigenenergies for  $\mathcal{PT}$ -unbroken eigenstates, enforcing a balance between gain and loss and thus probability conservation [1, 5, 6]. As such, it provides an ubiquitous route towards realizing exotic non-Hermitian phenomena in a stable manner, as demonstrated in optical [6–9], acoustic [10–13], circuit [14–16] and atomic platforms [17–22].

In this work, we found that beyond ensuring stability,  $\mathcal{PT}$  symmetry can also serve as a new paradigm for designing families of higher-dimensional non-Hermitian lattices with novel bulk, surface, hinge or corner dynamics. Previously, it was found that non-Hermitian lattices can possess robust localized modes not just due to topological protection, but also from the non-Hermitian skin effect (NHSE), where all eigenstates boundary accumulate exponentially under open boundary conditions (OBCs) [23–66]. In 2D or higher, topological localization and the NHSE can conspire to yield hybrid skin-topological modes [55–57, 60, 67–69]. New intricate phenomenology beyond 1D can also appear [37, 70–73], particularly defect NHSE at dislocations and disclinations [51–54], universal and geometry-dependent NHSE [62] and reduced effective dimensionality due to directional non-commutativity of the NHSE [65].

Our approach is based on the central observation that NHSE always requires a complex spectrum under periodic boundary conditions (PBCs) [33, 40, 41, 44], and hence broken  $\mathcal{PT}$  symmetry. Hence we can generate new classes of higher-dimensional NHSE phenomena by not breaking  $\mathcal{PT}$  symmetry globally, but by selectively “activating” or breaking it in different sectors e.g. edges

and surfaces. By systematically switching on/off various types of NHSE in higher-dimensional lattices, we obtain new families of non-Hermitian states beyond known higher-order topological, skin or hybrid states.

We start with 1D non-Hermitian topological models where  $\mathcal{PT}$  symmetry can be independently controlled for bulk and edge states, and use them as building blocks for higher dimensional lattices with selectively activated bulk and boundary NHSE. This unveils exotic NHSE phenomena in 2D, for instance (i) a directional NHSE toggling mechanism requiring a PBC direction (unlike conventional NHSE which always requires OBCs), (ii) an intrinsic hybrid skin-topological effect with NHSE-immune bulk independent of lattice geometry [62] and (iii) flow of states from one boundary to another without chiral or dynamical pumping. In 3D or higher,  $\mathcal{PT}$  symmetry can even conspire with  $\mathcal{CP}$  symmetry and hybrid higher-order topology to activate much richer arrays of non-Hermitian phenomena.

Note that NHSE manifests as boundary accumulation and changes the dimensionality of eigenstates. In the rest of this paper, we shall use the terms of bulk/surface/edge/hinge states to denote eigenstates that are adiabatically connected to them in the Hermitian limit to avoid confusion.

*Corner NHSE from non-Bloch  $\mathcal{PT}$  symmetry breaking.*— To provide a first illustration of  $\mathcal{PT}$ -activated NHSE modes, we consider a minimal 2D model  $H_{\gamma,2D}$  whose robust corner/edge modes are localized not from higher-order topology [74–77], but from the NHSE activated by  $\mathcal{PT}$  symmetry breaking. We construct  $H_{\gamma,2D}$  by extending the 1D non-Hermitian Su-Schrieffer-Heeger (nH-SSH) model to 2D with a  $k_y$ -dependent coupling [78–83] (also seen Supplemental Materials [84]):

$$H_{\gamma,2D}(k_x, k_y) = h_{\gamma}^{(0)} \sigma_0 + h_{\gamma}^{(x)} \sigma_x + h_{\gamma}^{(y)} \sigma_y \quad (1)$$

where  $h_{\gamma}^{(0)} = t_1 \cos k_y$ ,  $h_{\gamma}^{(x)} = u + v \cos k_x$  and  $h_{\gamma}^{(y)} = v \sin k_x + i\gamma/2 + it_2 \sin k_y$ , and  $\sigma_{\alpha=x,y,z}$  are the Pauli ma-

\* phylch@nus.edu.sg

† lilh56@mail.sysu.edu.cn

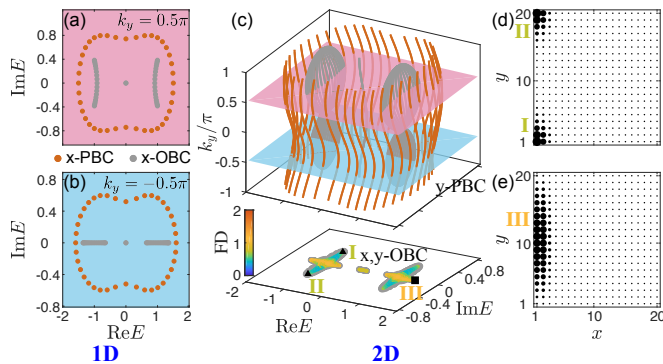


**Figure 1. Corner and edge modes activated by  $\mathcal{PT}$  symmetry breaking.** (a,b): The OBC spectrum (gray) of  $H_{\gamma,2D}$ , regarded as a 1D model with fixed  $k_y$ , can be (a) complex or (b) real depending on whether  $\mathcal{PT}$  symmetry is restored by the NHSE. For reference, the PBC spectrum (brown) is always complex. (c) Top: Full spectrum of  $H_{\gamma,2D}$  as a 2D model, with PBCs along the  $y$  direction. Pink and blue cross sections correspond to the spectra in (a) and (b). Bottom: The full  $x, y$ -OBC spectrum (colored according to the fractal dimension FD) is contained within the set of  $y$ -PBC eigenenergies summed over all  $k_y$  (gray). Corner modes with  $FD \approx 0$  (I,II triangles) are plotted in (d), and exist at  $\text{Im}(E) \neq 0$  where  $\mathcal{PT}$  symmetry is broken. An edge mode with  $FD \approx 1$  (square) exist at  $\text{Im}(E) = 0$ , as plotted in (e). Parameters are  $\gamma = 1.4$ ,  $t_1 = 0.1$ ,  $t_2 = 0.1$ ,  $v = 1$ , and  $u = 0.7$ .

trices acting on a pseudospin-1/2 space (e.g. two sublattices). Here  $u, v$  and  $t_1, t_2$  are hopping parameters along the  $x$  and  $y$  directions respectively.

First consider fixed  $k_y$ , when this Hamiltonian can be viewed as a 1D nH-SSH model with  $x$ -direction NHSE [80] (with an extra real energy shift of  $t_1 \cos k_y$ ). The non-Hermitian  $\gamma$  term breaks the  $\mathcal{PT}$  symmetry and makes the PBC spectrum (brown) complex (Fig. 1(a,b)). Under  $x$ -OBCs,  $\mathcal{PT}$  symmetry may continue to be broken as in Fig. 1(a) for  $k_y \in (0, \pi)$ , if the OBC spectrum (gray) is also complex. However,  $\mathcal{PT}$  symmetry may be restored in another parameter range  $k_y \in [-\pi, 0]$ , when the OBC spectrum (gray) becomes real (Fig. 1(b)) [84–86]. This selective restoration of  $\mathcal{PT}$  symmetry is possible because the NHSE amplifies states in a directed manner, and this amplification (and hence complex energies) may be blocked by a boundary.

In the 2D context, Figs. 1(a,b) correspond to 1D slices [pink and blue planes in Fig. 1(c)] of  $H_{\gamma,2D}$  at different quasi-momenta  $k_y$ , respectively with restored/broken non-Bloch  $\mathcal{PT}$  symmetry. When OBCs are also implemented in the  $y$ -direction,  $k_y$  is no longer diagonal and the spectrum with both  $x, y$ -OBCs [Fig. 1(c) Bottom] may differ from the  $x$ -OBC,  $y$ -PBC spectrum (Top). In particular,  $y$ -NHSE can occur only when the non-Bloch  $\mathcal{PT}$  symmetry is already broken, since the NHSE requires nontrivial spectral winding[33, 40, 41, 44], which in turn requires complex eigenenergies. Since  $x$ -NHSE acts on all eigenstates,  $H_{\gamma,2D}$ , there are no completely extended states; there are only edge or corner-localized states un-

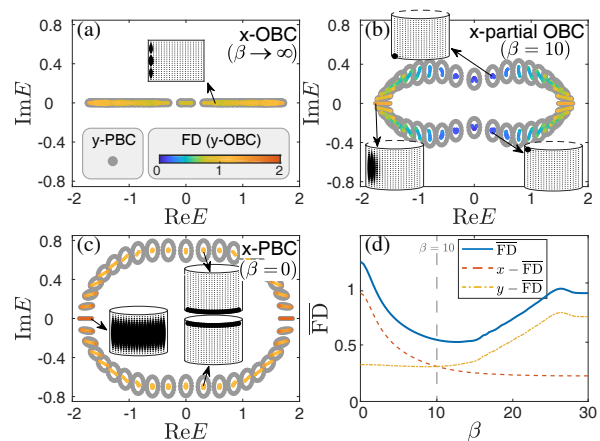


**Figure 2. Toggling between  $x$ -NHSE and  $y$ -NHSE through  $x$ -boundary tuning, without any parameter adjustment.** From (a) to (c): As we morph from  $x$ -OBC (a) to  $x$ -PBC (c), the  $y$ -PBC (gray) and  $y$ -OBC (colored by fractal dimension FD) spectra for  $H_{\gamma,2D}^\beta$  transitions from purely real to complex. Meanwhile, as activated by  $\mathcal{PT}$  symmetry breaking, the skin modes transition from  $x$  to  $y$ -edge localized ( $\overline{FD} \approx 1$ ), as plotted in the insets. Corner skin modes with  $FD \approx 0.5$  appear in the intermediate  $\beta \approx 10$  regime purely as a by-product of this  $\mathcal{PT}$  activation mechanism. (d) Average FD and its 1D projections as a function of  $\beta$  under the  $y$ -OBC, with the trough at  $\beta \approx 10$  indicative of corner localization. Parameters are  $\gamma = 1.4$ ,  $t_1 = 0.1$ ,  $t_2 = 0.1$ ,  $v = 1$ , and  $u = 0.9$  in all panels.

der full  $x, y$ -OBCs, corresponding to single/double direction NHSE from unbroken/broken non-Bloch  $\mathcal{PT}$  symmetry, as shown in Fig. 1(d) and (e) respectively. To quantify the effective dimensionality of these eigenstates  $\psi_{n,r}$ , we introduce the fractal dimension

$$FD = -\ln\left[\sum_{\mathbf{r}} |\psi_{n,r}|^4\right] / \ln \sqrt{N}, \quad (2)$$

$N$  being the total number of sites. We have  $FD \approx 0, 1$  or  $2$  for corner, edge and 2D bulk states. In Fig. 1(c) Bottom,  $FD \approx 1$  for states with real eigenenergies, indicating their 1D edge-localized nature [Fig. 1(e)]. In contrast, states with complex eigenenergies have  $FD$  closer to 0, corresponding to the corner localization in Fig. 1(d).

*Directional toggling of NHSE and symmetry-driven corner modes.*— Noting that  $\mathcal{PT}$  symmetry plays a crucial role in determining the allowed NHSE pumping directions, we now show that it can be used to “activate” the NHSE *exclusively* in the  $x$  or  $y$  directions. We call this directional NHSE toggling. Furthermore, at an intermediate stage of the toggling, localization exists briefly in both directions, leading to a novel mechanism for *symmetry-driven* corner modes.

To demonstrate this intriguing directional toggling of the NHSE, we tune the  $\mathcal{PT}$  symmetry by varying the boundary hoppings. We interpolate between  $x$ -PBCs and  $x$ -OBCs with a parameter  $\beta$ , such that  $H_{\gamma,2D}$  becomes

$$H_{\gamma,2D}^\beta = H_{\gamma,2D}^{\text{OBC}} + e^{-\beta} H_{1 \leftrightarrow N_x} \quad (3)$$

where  $H_{\gamma,2D}^{\text{OBC}}$  is the Hamiltonian under full  $x, y$ -OBCs, and  $H_{1 \leftrightarrow N_x}$  denotes the hoppings between the first and last unit cells along the  $x$ -direction [84].

We have  $x$ -OBCs and hence  $x$ -NHSE at  $\beta \rightarrow \infty$ , and if parameters are chosen such that the non-Bloch  $\mathcal{PT}$  symmetry is unbroken for all states, no  $y$ -NHSE can occur, even though we also have  $y$ -OBCs. (Corner NHSE shall occur otherwise, see Supplemental Materials [84].) This gives the  $x$ -edge-localized modes of Fig. 2(a), with  $\text{FD} \approx 1$ . By contrast, the other limit of  $\beta = 0$  recovers  $x$ -PBCs and leads to  $y$ -NHSE, leading to  $y$ -localized states [Fig. 2(c)]. In both scenarios, the  $y$ -OBCs remain unchanged yet, by adjusting the  $x$ -boundary hoppings, we can “activate” the localization in the  $y$ -direction through  $\mathcal{PT}$  symmetry.

Interestingly, with partial  $x$ -OBCs i.e.  $\beta = 10$ , corner modes can appear as an intermediate between  $x$  and  $y$ -boundary localization [Fig. 2(b)]. These corner modes are evidently distinct from known higher-order skin, topological or hybrid modes, which require proper full OBCs, and may in fact harbor enigmatic scale-free properties inherited from 1D partial boundary states [42, 43]. We note that some eigenstates always exist at real energies, and are thus always free from the  $y$ -NHSE.

To quantify the transition between skin localizations along the two directions, we present in Fig. 2(d) the average fractal dimension  $\overline{\text{FD}}$  and its 1D projections ( $\overline{\alpha\text{-FD}}$  and  $\overline{y\text{-FD}}$ ) over all states as functions of  $\beta$ , where

$$\alpha\text{-FD} = -\ln \left[ \sum_{\alpha} \left| \sum_{\alpha'} |\psi_{n,r}|^2 \right| \right] / \ln \sqrt{N} \quad (4)$$

with  $\alpha, \alpha' \in (x, y)$  and  $\alpha \neq \alpha'$ . Similar to the FD,  $\alpha\text{-FD}$  quantifies the locality along a single direction, which is 1 (0) for fully extended (localized) states along the  $\alpha$  direction. While  $\beta = 0$  and  $\beta \gg 1$  gives  $\overline{\text{FD}} \approx 1$ , a trough of  $\overline{\text{FD}}$  exists between them, indicative of corner localization during the transition between single-directional  $y$ -NHSE under  $x$ -PBC ( $\beta = 0$ ) and  $x$ -NHSE under  $x$ -OBC ( $\beta \rightarrow \infty$ ). Meanwhile,  $x\text{-FD}$  decreases and  $y\text{-FD}$  increases (almost) monotonously with  $\beta$ , reflecting the mutual exclusion of NHSE along  $x$  and  $y$  directions.

*Edge- $\mathcal{PT}$ -breaking and selective boundary NHSE.*— So far, we have only seen how non-Bloch  $\mathcal{PT}$  symmetry breaking can activate various NHSE channels for bulk states. We next discuss how that can interplay with non-trivial topology, which separately gives  $\mathcal{PT}$  symmetric topological edge modes. Specifically, we show that  $\mathcal{PT}$  can be selectively broken for edge states only, leading to a new type of boundary NHSE distinguished from the usual bulk NHSE. We introduce another 2D model

$$H_{g,2D} = \sum_{\alpha=0,x,y,z} h_g^{(\alpha)}(k_x, k_y) \sigma_{\alpha}, \quad (5)$$

where  $h_g^{(0)} = t_1 \cos k_y$ ,  $h_g^{(x)} = u + v \cos k_x$ ,  $h_g^{(y)} = v \sin k_x$ , and imaginary  $h_g^{(z)} = i(g + t'_2 \sin k_y)$ . This Hamiltonian satisfies the  $\mathcal{PT}$  symmetry [ $\mathcal{PT}, H_{g,2D}$ ] = 0 with  $\mathcal{PT} = \sigma_x \mathcal{K}$ . When  $u^2 + v^2 - 2uv > g + t'_2$  (all parameters chosen

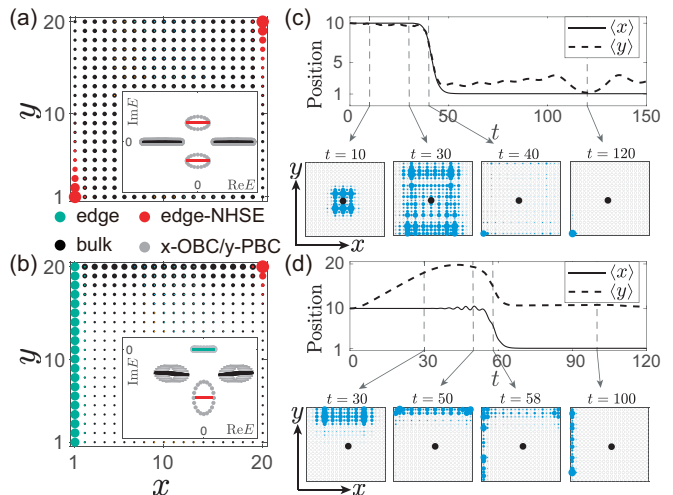


Figure 3. **Selective boundary NHSE and non-monotonic state dynamics.** (a)  $H_{g,2D}$  hosts  $\mathcal{PT}$ -unbroken bulk (black) and  $\mathcal{PT}$ -broken topological  $x$ -OBC/ $y$ -PBC edge states (gray). Under full OBCs, the latter experiences  $y$ -NHSE and become corner-localized (red). (b)  $H'_{g,2D}$  is deformed from  $H_{g,2D}$  such that  $\mathcal{PT}$  symmetry is restored for the branch of edge states (green) with  $\text{Im}(E) > 0$ , which remains edge-localized, at the expense of the bulk states (black), which is thus  $y$ -NHSE localized. (c,d) depicts the dynamical evolution of a center-localized initial state (black dot) due to  $H_{g,2D}$  and  $H'_{g,2D}$  respectively, with the size of blue dots indicating evolved state density. Qualitatively distinct stages occur before and after encountering the upper boundary; in (d), the upper edge state evolves into the left edge state, leading to non-monotonic  $\langle y \rangle$ . Parameters are  $u = 0.2$ ,  $g = 0.3$ ,  $t_1 = 0.3$  and  $t'_2 = 0.1$ , with system size  $N_x = N_y = 20$ .

to be positive), all bulk states are  $\mathcal{PT}$  unbroken and are free of any type of NHSE. On the other hand, the effective edge Hamiltonian read [87–90]:

$$H_{2D,\text{edge}}^{\pm} = \hat{P}_{\pm} H_{g,2D} \hat{P}_{\pm} = t_1 \cos k_y \pm i(g + t'_2 \sin k_y)$$

with  $\hat{P}_{\pm} = (1 \pm \sigma_z)/2$  the projectors of edge states. It is clear that  $H_{2D,\text{edge}}^{\pm}$  holds no  $\mathcal{PT}$  symmetry, and gives a complex edge spectrum [gray dotted loop in the inset of Fig. 3(a)] with nontrivial spectral winding for  $k_y \in (-\pi, \pi]$ . Consequently,  $y$ -NHSE occurs for these  $x$ -boundary states under  $y$ -OBCs, accumulating on opposite corners (red) depending on the sign of  $\text{Im}(E)$  [Fig. 3(a)]. This mechanism represents a type of hybrid skin-topological effect, namely that topological states are pushed to lower-dimensional boundaries by NHSE, yet bulk states remain extended [55]. Notably, the  $\mathcal{PT}$ -protected bulk spectrum remains purely real (Fig. 3(a)) and impervious to any NHSE throughout. Indeed, this absence of bulk NHSE is geometry-independent, representing an intrinsic hybrid skin-topological effect [84].

Going further, we may also selectively recover/break  $\mathcal{PT}$  symmetry and hence turn off/on the NHSE for different branches of edge states. Explicitly, by introducing

an extra anti-Hermitian term  $-i(t'_2 \sin k_y + g)\sigma_0$ :

$$H'_{g,2D} = H_{g,2D} - i(t'_2 \sin k_y + g)\sigma_0, \quad (6)$$

one branch of edge eigenenergies becomes real,  $H_{2D,edge}^+ \rightarrow H_{2D,edge}^{\prime+} = t_1 \cos k_y$ . As seen in Fig. 3(b), these edge states remain left edge-localized (green) under full OBCs because they cannot undergo additional NHSE, but those of the other branch are  $\mathcal{PT}$ -broken and collapse into corner modes (red) due to  $y$ -NHSE.

*Anomalous  $\mathcal{PT}$ -activated state dynamics.*— The selective activation of these various forms of corner and edge NHSE entails a competition between different NHSE channels, and interestingly gives rise to qualitative transitions in different stages of the state dynamics, distinguished to that of different bulk NHSE channels in  $H_{\gamma,2D}$  [84]. Consider an initial state  $|\psi(0)\rangle = (|\uparrow, N_x/2, N_y/2\rangle + |\downarrow, N_x/2, N_y/2\rangle)/\sqrt{2}$  localized at the center of an  $N_x \times N_y$  lattice. We dynamically evolve it via  $|\psi(t)\rangle = e^{-iHt}|\psi(0)\rangle$  and investigate the evolution of its center-of-mass  $\langle x \rangle$  and  $\langle y \rangle$  in Figs. 3(c) and (d), for  $H = H_{g,2D}$  and  $H'_{g,2D}$  from Eqs. (5) and (6) respectively.

For  $H = H_{g,2D}$  (Fig. 3(c)), both  $\langle x \rangle$  and  $\langle y \rangle$  remain roughly constant for a short time, since  $|\psi(t)\rangle$  is governed by NHSE-free bulk dynamics [see Fig. 3(a)] before it encounters a boundary. After  $t \approx 30$ , the state arrives at the boundary and the intrinsic hybrid skin-topological effect is activated. The dynamics are then dominated by the corner states with  $\text{Im}(E) > 0$ , where  $\langle x \rangle, \langle y \rangle \approx 1$ .

More interestingly,  $\langle x \rangle$  and  $\langle y \rangle$  can evolve non-monotonically in the dynamics governed by  $H'_{g,2D}$ , which possesses bulk  $y$ -NHSE and a skin-free branch of edge states (green in Fig. 3(b)). Due to bulk  $y$ -NHSE, the state is initially symmetrically pushed to the top boundary, and  $\langle y \rangle$  increases while  $\langle x \rangle$  remains constant, as shown in Fig. 3(d). After encountering the top boundary at  $t \approx 50$ , the dynamics become dominated by the left edge states with  $\text{Im}(E) > 0$ , and the  $y$ -NHSE is effectively deactivated. As such, the edge state “flows” from the top to the left boundary, and  $\langle x \rangle \rightarrow 1$  and  $\langle y \rangle \rightarrow N_y/2$ . This enigmatic behavior is possible because the left edge states are  $\mathcal{PT}$ -protected and do not undergo any NHSE to become corner states.

*3D generalizations of  $\mathcal{PT}$ -activated NHSE.*— The various avenues for  $\mathcal{PT}$ -activated NHSE effects discussed above takes on even richer possibilities in higher dimensions. Below, we briefly demonstrate how they acquire new interpretations as surface and hinge-selective NHSE in 3D. Specifically, we consider a 3D Hamiltonian of the form

$$H_{\gamma/g,3D}(\mathbf{k}) = H_{\gamma/g,0}(k_x, k_y) + (u' + v' \cos k_z)\sigma_0\tau_x + v' \sin k_z\sigma_0\tau_y \quad (7)$$

with  $\tau_{x,y,z}$  another set of Pauli matrices.  $H_{\gamma/g,0}(k_x, k_y)$  is inherited from the previous  $\mathcal{PT}$ -breaking and directional toggling NHSE models  $H_{\gamma/g,2D}$ :

$$H_{\gamma,0} = i[(u + v \cos k_x)\sigma_x + v \sin k_x\sigma_y + t_1 \cos k_y\sigma_0]\tau_z - (\gamma/2 + t_2 \sin k_y)\sigma_y\tau_0, \quad (8)$$

$$H_{g,0} = iH_{g,2D}\tau_z. \quad (9)$$

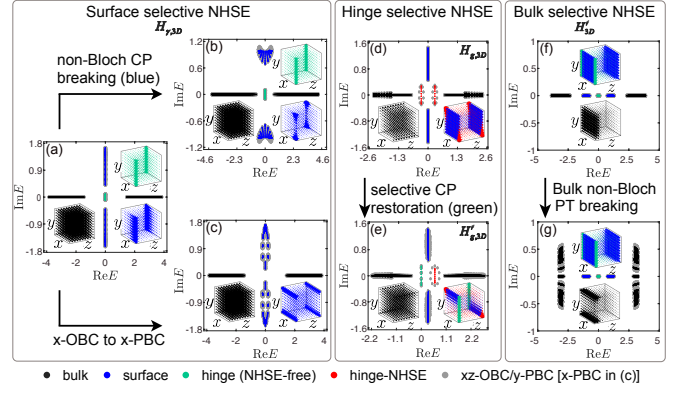


Figure 4. **NHSE selectively activated by  $\mathcal{PT}$  or  $\mathcal{CP}$  symmetry breaking in 3D.** In most panels [except for (c) with  $x$ -PBC], colored dots represent the bulk, surface or hinge spectra under full OBCs, and gray dots represent the  $xy$ -OBC/ $z$ -PBC spectra. Insets display the average spatial distribution of eigenstates of the respective color. (a,b,c), (d), (e), and (f,g) pertain to  $H_{\gamma,3D}$ ,  $H_{g,3D}$ ,  $H'_{g,3D}$ , and  $H'_{3D}$  respectively. In (a,b,c), the topologically (001) and (00 $\bar{1}$ )-surface localized states (blue) experience corner pumping from  $\mathcal{CP}$ -breaking (b) or  $x$  to  $y$ -NHSE directional toggling (c). In (d,e), the hinge-localized states (red) can have  $\mathcal{CP}$  symmetry selectively broken (unbroken), respectively resulting in corner (red) or edge (green) localization. In (f,g), on-demand switching of 1st and 2nd-order 3D bulk NHSE (black surface and edges) through  $\mathcal{PT}$  breaking leaves other states (green,blue) invariant. In (a) to (c), parameters are  $v = 1$ ,  $u' = 0.6$ ,  $v' = 3$  and  $t_1 = t_2 = 0.1$ , with  $u = 0.6$  and  $\gamma = 0.4$  for (a) and (c);  $u = 0.5$  and  $\gamma = 1.4$  for (b). In (d) and (e), parameters are  $u = 0.2$ ,  $v = 1$ ,  $u' = 0.4$ ,  $v' = 2$ ,  $g = 0.3$ ,  $t_1 = 0.3$  and  $t_2 = 0.1$ . In (f) and (g), parameters are  $u' = 0.2$ ,  $v' = 1$ ,  $v = 3$ ,  $\gamma = 1.4$  and  $t_1 = t_2 = 0.1$ , with  $u = 0.9$  for (f) and  $u = 0.5$  for (g).

Under  $z$ -OBCs,  $\tau_0$  and  $\tau_z$  terms serve as overall and (001)-(00 $\bar{1}$ )-surface energy offsets respectively, and the surface states obey the effective Hamiltonian  $H_{\pm, \text{surface}} = \hat{P}_{\pm, 3D} H_{\gamma/g, 3D} \hat{P}_{\pm, 3D}$  with  $\hat{P}_{\pm, 3D} = (1 \pm \sigma_0 \tau_z)/2$   $z$ -surface state projectors [87–90]. Note that the choices  $H_{\gamma/g,0}$  are not unique, and the explicit forms in Eqs. (8) and (9) are chosen to restore  $\mathcal{PT}$  symmetry

$$[\sigma_x \tau_x \mathcal{K}, H_{\gamma/g,3D}(\mathbf{k})] = 0. \quad (10)$$

Also, an additional charge-parity ( $\mathcal{CP}$ ) symmetry emerges for the surface states [84, 91], which offers another avenue for eliminating the NHSE by ensuring purely imaginary eigenenergies.

Our numerical results for these 3D models are shown in Fig. 4, where eigenmodes are marked with different colors according to their corresponding sectors and boundary conditions. In Fig. 4(a,b,c) for  $H_{\gamma,3D}$ , the (001) and (00 $\bar{1}$ ) surface states essentially recapitulate the symmetry-selected and directional toggling NHSE effects of Figs. 1 and 2. Going from Fig. 4(a) to (b), these surface states (blue) become corner-localized due to non-Bloch  $\mathcal{CP}$ -breaking, analogous to the corner localization Fig. 1(d) due to  $\mathcal{PT}$ -breaking, while bulk (black) and

hinge (green) states remain unchanged. Likewise, directional toggling from  $x$ -NHSE to  $y$ -NHSE localization occurs when the  $x$ -OBC of Fig. 4(a) is replaced by the  $x$ -PBC of Fig. 4(c).

Similarly, the surface (blue) and hinge (red) states on (001) and (00 $\bar{1}$ ) surfaces of  $H_{g,3D}$  in Fig. 4(d) are in direct correspondence with the bulk (black) and boundary (red) states of  $H_{g,2D}$  in Fig. 3(a). Meanwhile, bulk eigenenergies remain real as our choice of parameters maintains unbroken  $\mathcal{PT}$  symmetry in Eq. (7). In analogy with  $H'_{g,2D}$  in Fig. 3(b), a  $\mathcal{CP}$  symmetry can be recovered in one branch of hinge states on each of (001) and (00 $\bar{1}$ ) surfaces by introducing an extra Hermitian term to the Hamiltonian, i.e.  $H'_{g,3D}(\mathbf{k}) = H_{g,3D}(\mathbf{k}) + (t_2 \sin k_y + g)\sigma_0\tau_0$ , which removes the NHSE on these hinge states [Fig. 3(b)].

Alternatively, a 3D Hamiltonian with only bulk-NHSE can be designed such that its bulk (PBC) states are not  $\mathcal{PT}$ -symmetric, but that non-Bloch  $\mathcal{PT}$ -symmetry can be recovered in certain parameter regimes, for instance  $H'_{3D}(\mathbf{k}) = H_{\gamma,2D}(k_z, k_y) \otimes \tau_0 + \sigma_z \otimes H_{SSH}(k_x)$ , with

$$H_{SSH}(k_x) = (u' + v' \cos k_x)\tau_x + v' \sin k_x \tau_y \quad (11)$$

the Hermitian SSH model and  $H_{\gamma,2D}(k_z, k_y)$  from Eq. (1). Consequently, bulk states accumulate to a 2D surface (or 1D hinges) when the non-Bloch  $\mathcal{PT}$  symmetry is unbroken (or broken), as shown in Fig. 4(f,g). In contrast to  $H_{\gamma/g,3D}$ , conventional surface (blue) or hinge (green) states are immune from the NHSE and remain extended.

*Discussion.*—  $\mathcal{PT}$  symmetry ensures real spectra, thus eliminating the prospect for spectral winding. This fundamental observation leads to the new paradigm of  $\mathcal{PT}$ -activated NHSE, where new families of NHSE-related phenomena can be designed by selectively symmetry breaking in bulk or boundary subspaces. In 2D, we discussed novel directional NHSE toggling and  $\mathcal{PT}$ -mediated corner modes, as well as selective edge- $\mathcal{PT}$  breaking and restoring that causes non-monotonic transfer of edge states. In 3D or higher,  $\mathcal{PT}$  activation leads to far more varied phenomenology by interplaying with the already rich classes of higher-order hybrid skin-topological modes. This paradigm of symmetry-controlled NHSE can be extended to include other symmetries which forbid spectral winding, such as  $\mathcal{CP}$  symmetry or pseudo-Hermiticity.

Since  $\mathcal{PT}$ -activated NHSE is fundamentally a phenomenon on a linear lattice, it can be experimentally demonstrated on any metamaterial or artificial lattice, whether classical or quantum, as long as  $\mathcal{PT}$  symmetry can be broken through a combination of gain/loss and non-reciprocity. Possible platforms include non-reciprocal lossy acoustic or photonic crystals or waveguides [92–95], ultracold atomic lattices [96], superconducting quantum circuit lattices [97–107], and in particular op-amp controlled electrical circuits which can be constructed with great versatility [16, 67, 108–114].

## CONTENTS

I. Non-Hermitian SSH model	6
II. Non-Bloch $\mathcal{PT}$ symmetry	7
III. The explicit form of Hamiltonian $H_{\gamma,2D}^\beta$	8
IV. Further results of $H_{\gamma,2D}$	9
A. Corner NHSE in the non-Bloch $\mathcal{PT}$ broken regime	9
B. Evolution process for $H_{\gamma,2D}$ with mutual exclusively or conventional NHSE	10
V. Geometry-independence of the intrinsic hybrid skin-topological effects	11
VI. Effective surface Hamiltonian for 3D generalizations	11
References	12

## Supplementary Materials

## I. NON-HERMITIAN SSH MODEL

The models supporting various types of NHSE discussed in the main text are mostly designed based on a non-Hermitian Su-Schrieffer-Heeger (SSH) model, described by the Hamiltonian [83]:

$$H(k_x) = \sum_{\alpha=x,y,z} h_\alpha(k_x) \sigma_\alpha, \quad (\text{S1})$$

where  $h_x(k_x) = u + v \cos k_x$ ,  $h_y(k_x) = v \sin k_x + i\gamma/2$ ,  $h_z = ig$ , and  $\sigma_{\alpha=x,y,z}$  is the Pauli matrix acting on a pseudospin-1/2 space [e.g. two sublattices  $|A\rangle$  and  $|B\rangle$ ] as shown in Fig. S1(a).  $u$  and  $v$  denote the Hermitian staggered hopping amplitudes. The two non-Hermitian parameters  $\gamma$  and  $g$  describes asymmetric hoppings and on-site gain and loss respectively, as illustrated in Fig. S1(a). By separately tuning the two non-Hermitian parameters  $g$  and  $\gamma$ , we can break or restore  $\mathcal{PT}$ -symmetry selectively for bulk or topological edge states in this model, as discussed below.

When  $\gamma = 0$ , non-Hermiticity enters the Hamiltonian only through the on-site gain and loss of  $g$ , and the resultant Hamiltonian

$$H_g \equiv H(\gamma = 0)$$

holds a  $\mathcal{PT}$  symmetry:  $[\mathcal{PT}, H_g] = 0$  with  $\mathcal{PT} = \sigma_x \mathcal{K}$  and  $\mathcal{PT}^2 = +1$ . A nonzero  $g$  does not break the  $\mathcal{PT}$  symmetry as the gain and loss are balanced between sublattices. As shown in Fig. S1(b), in the  $\mathcal{PT}$ -unbroken phase, all bulk states have real eigenenergies since they are also eigenstates of  $\mathcal{PT}$  symmetry operator [1, 2]. On the other hand, topological edge states for the SSH model are sublattice polarized and hence  $\mathcal{PT}$ -broken. Instead of being eigenstates of  $\mathcal{PT}$  symmetry operator, these states are related to each other through the symmetry, i.e.  $\mathcal{PT}|\psi_+\rangle \propto |\psi_-\rangle$ , with  $|\psi_{+,-}\rangle$  the topological edge states localized at left and right ends respectively. The sublattice-polarization of these edge states allow us to write down their effective Hamiltonians through projectors  $\hat{P}_\pm = (1 \pm \sigma_z)/2$ , i.e.

$$H_{\text{edge}}^\pm = \hat{P}_\pm H_g \hat{P}_\pm = \pm ig,$$

which directly give their eigenenergies [87–90].

For the other non-Hermitian scenario of Eq. (S1) with  $g = 0$  but  $\gamma \neq 0$ ,

$$H_\gamma \equiv H(g = 0) \quad (\text{S2})$$

the  $\mathcal{PT}$  symmetry is broken, and the resultant complex bulk spectrum is known to have nontrivial spectral winding topology under the PBC, a signature of the emergence of NHSE under the OBC [39–41]. Yet its OBC bulk spectrum become real in Fig. S1(c) due to the recovery of a non-Bloch  $\mathcal{PT}$  symmetry [86, 115] or a pseudo-Hermiticity [4]. Explicitly, the OBC bulk spectrum can be described by a non-Bloch Hamiltonian  $\bar{H}_\gamma(k_x) = H_\gamma(k_x + i\kappa)$  with  $\kappa = \ln \sqrt{|(u + \gamma/2)/(u - \gamma/2)|}$  [32, 33, 80]. This Hamiltonian  $\bar{H}_\gamma(k_x)$  satisfies a non-Bloch  $\mathcal{PT}$  symmetry,

$$[\eta \mathcal{K}, \bar{H}_\gamma] = 0$$

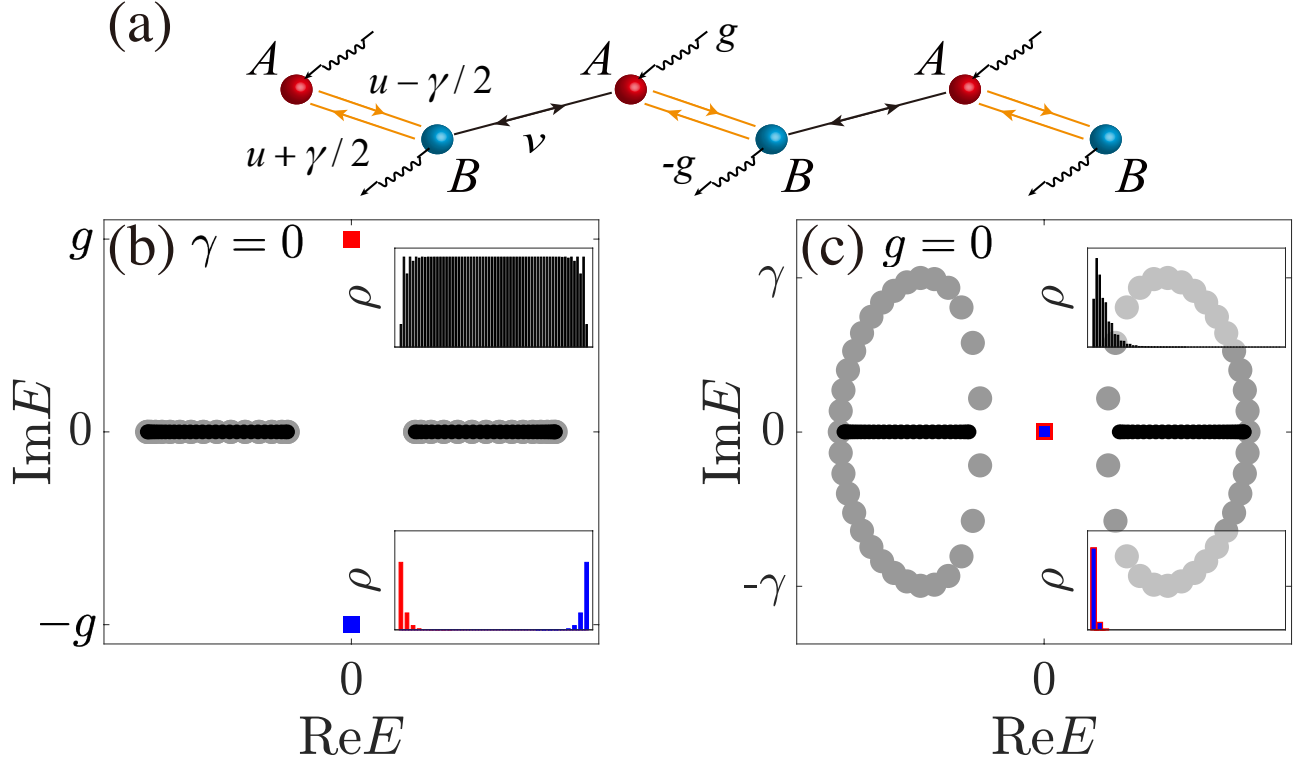


Figure S1. (color online). **The non-Hermitian SSH model.** (a) A sketch of the model of Eq. (S1), with  $\gamma$  ( $g$ ) the asymmetric hopping (gain/loss) parameter. (b) Typical PBC (gray) and OBC (other colors) spectra of  $H_g$ . Under the OBCs, bulk states can be  $\mathcal{PT}$ -symmetric and have real eigenenergies (black), but edge states are  $\mathcal{PT}$ -broken and have imaginary eigenenergies  $\pm ig$ . Insets demonstrate the spatial distribution of corresponding eigenstates. (c) Typical PBC and OBC spectra of  $H_\gamma$ , with the same color marks as in (b). The PBC spectrum in (c) is  $\mathcal{PT}$ -broken and possesses a nontrivial spectral winding, leading to a boundary accumulation of all eigenstates (see insets). The OBC spectrum restores a non-Bloch  $\mathcal{PT}$  symmetry and becomes purely real. Parameters are chosen to be  $u = 0.5$ ,  $v = 1$ , and (b)  $g = 0.2$ , (c)  $\gamma = 0.2$  for demonstration.

with  $\eta$  a  $k$ -dependent unitary operator, which is unbroken for all non-Bloch eigenstates when  $|u| > |\gamma/2|$  (as shown in Sec II of Supplement Materials). In contrast, here the topological edge states always remain  $\mathcal{PT}$ -symmetric and possess real (zero) eigenenergies, as a nonzero  $\gamma$  does not enter their effective Hamiltonian:

$$H_{\text{edge}}^\pm = \hat{P}_\pm H_\gamma \hat{P}_\pm = 0.$$

Note that the localizing direction of these edge states may be altered by the NHSE, yet their distributing dimensionality remains unchanged, namely they are always 0D edge states except for some critical points in the parameter space [116]. Similarly, edge states of 2D generalization Hamiltonian  $H_{\gamma,2D}$  with selective bulk NHSE, namely those near zero energy in Fig.1(c) and Fig.2(a) of the main text, are seen to also possess real eigenenergies with their distributing dimensionality unchanged by NHSE.

## II. NON-BLOCH $\mathcal{PT}$ SYMMETRY

In this section, we discuss the non-Bloch  $\mathcal{PT}$  symmetry of the non-Hermitian SSH model with asymmetric hoppings  $H_\gamma(k_x)$  of Eq.(S2). Its corresponding non-Bloch Hamiltonian reads [32, 33, 80]

$$\bar{H}_\gamma(k_x) = H_\gamma(k_x + i\kappa) = (A + iB)\sigma_x + (C + iD)\sigma_y, \quad (\text{S3})$$

with

$$\begin{aligned} A &= u + v \frac{\cos k_x}{2} \left( \sqrt{\left| \frac{u - \gamma/2}{u + \gamma/2} \right|} + \sqrt{\left| \frac{u + \gamma/2}{u - \gamma/2} \right|} \right), \quad B = v \frac{\sin k_x}{2} \left( \sqrt{\left| \frac{u - \gamma/2}{u + \gamma/2} \right|} - \sqrt{\left| \frac{u + \gamma/2}{u - \gamma/2} \right|} \right), \\ C &= v \frac{\sin k_x}{2} \left( \sqrt{\left| \frac{u - \gamma/2}{u + \gamma/2} \right|} + \sqrt{\left| \frac{u + \gamma/2}{u - \gamma/2} \right|} \right), \quad D = -v \frac{\cos k_x}{2} \left( \sqrt{\left| \frac{u - \gamma/2}{u + \gamma/2} \right|} - \sqrt{\left| \frac{u + \gamma/2}{u - \gamma/2} \right|} \right) + \frac{\gamma}{2}. \end{aligned} \quad (\text{S4})$$

To identify the non-Bloch  $\mathcal{PT}$  symmetry, we rewrite the non-Bloch Hamiltonian as

$$H_\gamma(k_x + i\kappa) = h'_x \sigma'_x + h'_y \sigma'_y \quad (\text{S5})$$

with

$$\begin{aligned} h'_x &= \frac{(A + iB)C - (C + iD)iB}{\sqrt{C^2 - B^2}}, \quad h'_y = \frac{(A + iB)iB + (C + iD)C}{\sqrt{C^2 - B^2}}, \\ \sigma'_x &= \frac{C}{\sqrt{C^2 - B^2}} \sigma_x - \frac{iB}{\sqrt{C^2 - B^2}} \sigma_y, \quad \sigma'_y = \frac{iB}{\sqrt{C^2 - B^2}} \sigma_x + \frac{C}{\sqrt{C^2 - B^2}} \sigma_y. \end{aligned} \quad (\text{S6})$$

It is straightforward to check that  $h'_x, h'_y \in \mathbb{R}$ ,  $(\sigma'_x)^2 = (\sigma'_y)^2 = \sigma_0$ , and  $\sigma'_x \sigma'_y \sigma'_x = -\sigma'_y$ . Therefore we obtain

$$[\eta \mathcal{K}, H_\gamma(k_x + i\kappa)] = 0 \quad (\text{S7})$$

with  $\eta = \sigma'_x$  a unitary operator and  $(\eta \mathcal{K})^2 = 1$ , indicating the non-Bloch  $\mathcal{PT}$  symmetry. Note that  $B$  and  $C$  are  $k_x$ -dependent coefficients, thus  $\eta$  also varies with  $k_x$ , represents a special form of pseudo-Hermiticity [4].  $\eta$  is ill-defined when  $|u| = |\gamma/2|$ , which is also the the boundary between non-Bloch  $\mathcal{PT}$  unbroken and broken phases. Specifically, the eigenenergies of  $H_\gamma(k_x + i\kappa)$  are given by

$$E_\gamma = \pm \sqrt{A^2 + C^2 - B^2 - D^2 - 2i(AB + CD)}, \quad (\text{S8})$$

and the unbroken phase requires  $AB + CD = 0$  and  $A^2 + C^2 - B^2 - D^2 \geq 0$  for  $\forall k_x \in (-\pi, \pi]$ . The first condition gives

$$AB + CD = v \frac{\sin k_x}{2} (\text{sgn}[u + \gamma/2] - \text{sgn}[u - \gamma/2]) \sqrt{|u^2 - \gamma^2/4|} = 0, \quad (\text{S9})$$

which is satisfied either when  $|u| > |\gamma/2|$ , or when  $k_x \in \{0, \pi\}$ . The second condition gives

$$A^2 + C^2 - B^2 - D^2 = u^2 + v^2 - \gamma^2/4 + v \cos k_x (\text{sgn}[u + \gamma/2] + \text{sgn}[u - \gamma/2]) \sqrt{|u^2 - \gamma^2/4|} \geq 0. \quad (\text{S10})$$

When  $|u| > |\gamma/2|$ , it reduces to  $u^2 + v^2 - \gamma^2/4 + 2v \cos k_x \sqrt{|u^2 - \gamma^2/4|} \geq (\sqrt{|u^2 - \gamma^2/4|} - v)^2 \geq 0$  and is always satisfied. In the non-Bloch  $\mathcal{PT}$  broken phase with  $|u| < |\gamma/2|$ , this condition may also hold as long as  $u^2 + v^2 \geq \gamma^2/4$ . Combining these results, the non-Bloch  $\mathcal{PT}$  is unbroken when  $|u| > |\gamma/2|$  with all  $E_\gamma$  being real, partially broken when  $u^2 + v^2 > \gamma^2/4 > u^2$  where only  $E_\gamma(k_x \in \{0, \pi\})$  are real, and fully broken where all bulk states acquire imaginary eigenenergies when  $\gamma^2/4 > u^2 + v^2$ .

### III. THE EXPLICIT FORM OF HAMILTONIAN $H_{\gamma,2D}^\beta$

In this section, we give the explicit form of  $H_{\gamma,2D}^\beta$  in Eq.(3) of the main text. According to this definition, the Hamiltonian  $H_{\gamma,2D}^\beta$  contains two parts: the Hamiltonian  $H_{\gamma,2D}$  in Eq.(1) of the main text under full OBCs, and its hopping between boundaries along  $x$ -direction. The first part reads

$$\begin{aligned} H_{\gamma,2D}^{\text{OBC}} &= \frac{v}{2} \sum_j^{N_x-1} \sum_k^{N_y} [\hat{\psi}_{j,k}^\dagger (\sigma_x - i\sigma_y) \hat{\psi}_{j+1,k} + \text{H.c.}] \\ &\quad + \frac{1}{2} \sum_j^{N_x} \sum_k^{N_y-1} [t_1 (\hat{\psi}_{j,k}^\dagger \hat{\psi}_{j,k+1} + \text{H.c.}) - it_2 (i\hat{\psi}_{j,k}^\dagger \sigma_y \hat{\psi}_{j,k+1} + \text{H.c.})] \\ &\quad + \sum_j^{N_x} \sum_k^{N_y} \hat{\psi}_{j,k}^\dagger (u\sigma_x + \frac{i\gamma}{2} \sigma_y) \hat{\psi}_{j,k}, \end{aligned} \quad (\text{S11})$$

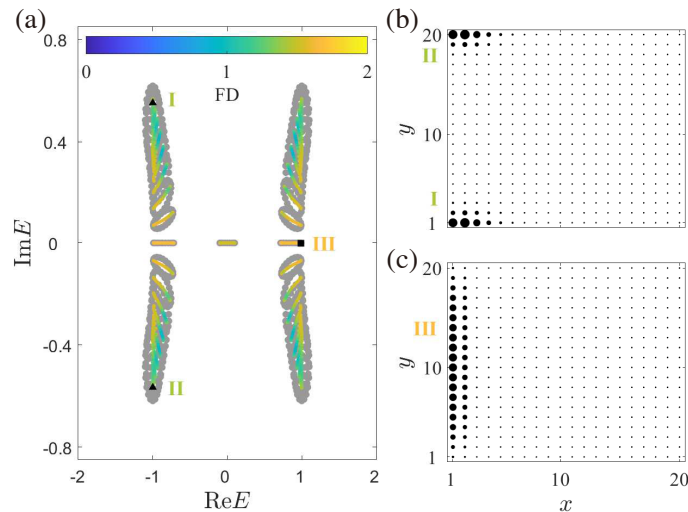


Figure S2. (color online). **The spectrum and distribution of a single eigenstate of  $H_{\gamma,2D}$  with corner NHSE.** (a)  $x$ -OBC/ $y$ -PBC (gray) and full OBCs (colored) spectra. Different colors indicate the FD of each eigenstate. (b) and (c) the distributions of eigenstates under full OBCs indexed by triangles and square in (a), respectively. In all panels, the parameters are chosen as  $\gamma = 1.4$ ,  $t_1 = t_2 = 0.1$ ,  $v = 1$ , and  $u = 0.5$ , and full OBCs.

where  $\hat{\psi}_{j,k} = [\hat{a}_{j,k}, \hat{b}_{j,k}]^T$ , with  $\hat{a}_{j,k}$  ( $\hat{b}_{j,k}$ ) being the annihilate operator for the pseudospin- $\uparrow$  ( $\downarrow$ ) [sublattices  $A$  ( $B$ )] on the  $(j, k)$ -th unit cell.

Similarly, the hoppings between boundaries along  $x$ -direction  $H_{1\leftrightarrow N_x}$  and  $y$ -direction  $H_{1\leftrightarrow N_y}$  are

$$H_{1\leftrightarrow N_x} = \frac{v}{2} \sum_k^{N_y} [\hat{\psi}_{N_x,k}^\dagger (\sigma_x - i\sigma_y) \hat{\psi}_{1,k} + \text{H.c.}], \quad (\text{S12})$$

$$H_{1\leftrightarrow N_y} = \frac{1}{2} \sum_j^{N_x} [t_1 (\hat{\psi}_{j,N_y}^\dagger \hat{\psi}_{j,1} + \text{H.c.}) - it_2 (i\hat{\psi}_{j,N_y}^\dagger \sigma_y \hat{\psi}_{j,1} + \text{H.c.})]. \quad (\text{S13})$$

Thereby, the Hamiltonian under full PBCs can be expressed by

$$H_{\gamma,2D}^{\text{PBC}} = H_{\gamma,2D}^{\text{OBC}} + H_{1\leftrightarrow N_x} + H_{1\leftrightarrow N_y}. \quad (\text{S14})$$

Through the Fourier transformation, the momentum space Hamiltonian  $H_{\gamma,2D}(k_x, k_y)$  in Eq.(1) of the main text can be obtained. In Eq.(3) of the main text, an extra factor  $e^{-\beta}$  is introduced to describe the partial OBCs along  $x$  direction.

## IV. FURTHER RESULTS OF $H_{\gamma,2D}$

### A. Corner NHSE in the non-Bloch $\mathcal{PT}$ broken regime

In the main text, we have discussed the 2D Hamiltonian  $H_{\gamma,2D}$  in the non-Bloch  $\mathcal{PT}$  symmetry unbroken (Fig.2 of the main text) and intermediate regime (Fig.1 of the main text), where non-Bloch  $\mathcal{PT}$  symmetry is unbroken for either all or some values of  $k_y$ . In this section, we discuss another situation where the non-Bloch  $\mathcal{PT}$  symmetry is partially broken [ $u^2 + v^2 > (\gamma + 2t_2 \sin k_y)^2/4 > u^2$ ] for *all* values of  $k_y$ .

In this regime, almost all bulk states become corner-skin states under the full OBCs, as shown in Fig. S2(a) and S2(b). The only exceptions are a  $\mathcal{O}(L)$  number of states falling on the real axis of the complex energy plane, which are extended along  $y$  direction [Fig. S2(c)]. This is because these states correspond to those with  $k_x \in \{0, \pi\}$  of the 1D non-Bloch Hamiltonian  $\bar{H}_\gamma(k_x)$ , which remains non-Bloch  $\mathcal{PT}$  unbroken even in the non-Bloch  $\mathcal{PT}$  broken phase (See Sec. II of Supplement materials).

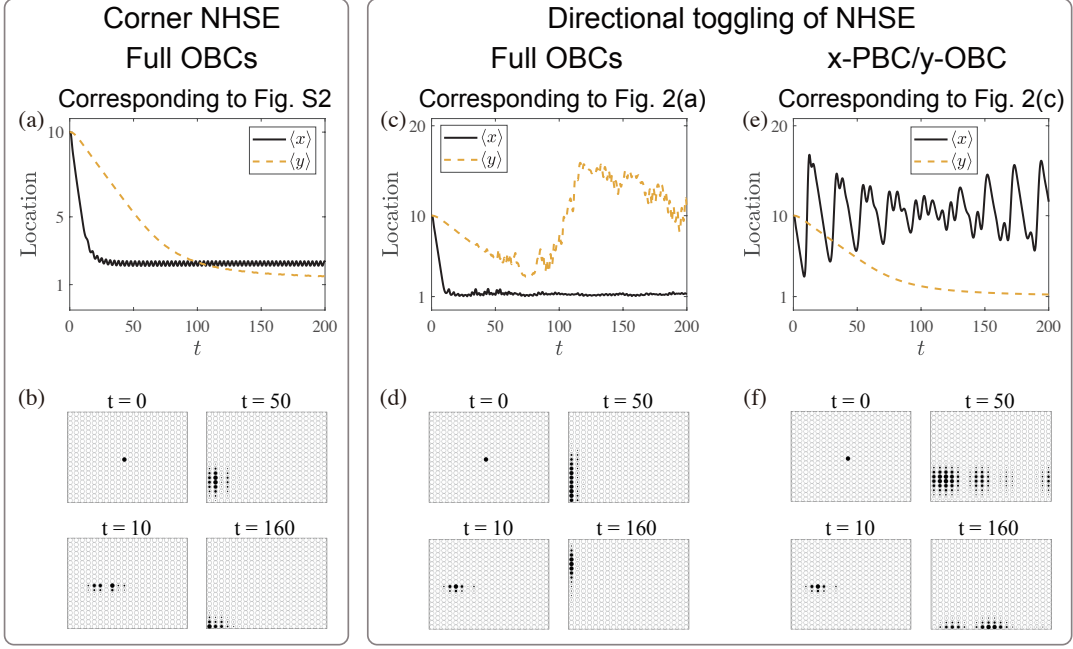


Figure S3. (color online). **The dynamical process for Hamiltonian  $H_{\gamma,2D}$  with various types of NHSE.** (a), (c), and (e) The mean position of states  $\langle x \rangle$  and  $\langle y \rangle$  during the evolution process. Here the initial state is prepared in the center of the 2D lattices. (b), (d), and (f) The normalized distribution of the state  $|\psi(t)\rangle$  at different time. In (a) and (b), parameters are  $\gamma = 1.4$ ,  $t_1 = t_2 = 0.1$ ,  $v = 1$ ,  $u = 0.5$ , the same as in Fig. S2 where corner NHSE occurs. (c) to (f) have the same parameters except for  $u = 0.9$ , the same as in Fig. 2 of the main text corresponding to non-Bloch  $\mathcal{PT}$  unbroken phase. The boundary conditions are chosen to be full OBCs in (a) to (d), and  $x$ -PBC/ $y$ -OBC in (e) and (f). In all panels the system's size is  $N_x = N_y = 20$ .

## B. Evolution process for $H_{\gamma,2D}$ with mutual exclusively or conventional NHSE

In this section, we discuss the evolution process governed by Hamiltonian  $H_{\gamma,2D}$ . As in the main text, here the initial state is also chosen to be  $|\psi(0)\rangle = (|\uparrow, x_0, y_0\rangle + |\downarrow, x_0, y_0\rangle) / \sqrt{2}$  with  $(x_0, y_0) = (N_x/2, N_y/2)$ , and the state at time  $t$  is given by  $|\psi(t)\rangle = e^{-iH_{\gamma,2D}t}|\psi(0)\rangle$ .

We first discuss the regime  $u < \gamma/2 - t_2$  where the non-Bloch  $\mathcal{PT}$  symmetry is broken and almost all bulk state suffer from corner NHSE. Specifically, bulk states with positive imaginary energy (which shall dominate the dynamics) locate at the bottom left corner, as discussed in Sec IV A and shown in Fig. S2(a) and S2(b). As a result,  $\langle x \rangle$  and  $\langle y \rangle$  decreases rapidly to  $\sim 1$ , as shown in Fig. S3(a). Figure S3(b) further demonstrates the distribution of  $|\psi(t)\rangle$  at different values of  $t$ .

In contrast, bulk states of this model locates at left edge under full OBCs when the non-Bloch  $\mathcal{PT}$  symmetry is unbroken, as shown in Fig.2(a) in the main text. Correspondingly,  $\langle x \rangle$  decreases rapidly while  $\langle y \rangle$  does not show a clear increasing or decreasing tendency, as shown in Fig. S3(c). Consistently, a state prepared deep in the bulk will evolve to the left boundary and remain there in a long-time dynamics, as shown in Fig. S3(d).

Finally, we demonstrate the dynamics for the same parameters as in Fig. S3(c) and (d), but with  $x$ -PBC/ $y$ -OBC instead of full OBCs. As discussed in the main text, a  $y$ -NHSE shall emerge in this scenario. Specifically, bulk states with positive imaginary parts distribute along the bottom edge, as shown in Fig.2(c) of the main text. Therefore, after replacing  $x$ -OBC with  $x$ -PBC,  $\langle y \rangle$  decreases rapidly while  $\langle x \rangle$  oscillates around  $N_x/2$ , as shown in Fig. S3(e). More explicitly, evolution of a state behaves the same under the full OBCs and  $x$ -PBC/ $y$ -OBC before it reaches a boundary of the system, as shown in Fig. S3(d) and Fig. S3(f) with  $t = 10$ . Afterward, different boundary conditions lead to distinct dynamical behaviors, and  $|\psi(t)\rangle$  remains in the bottom boundary in a long-time dynamics for the system under  $x$ -PBC/ $y$ -OBC [Fig. S3(f)].

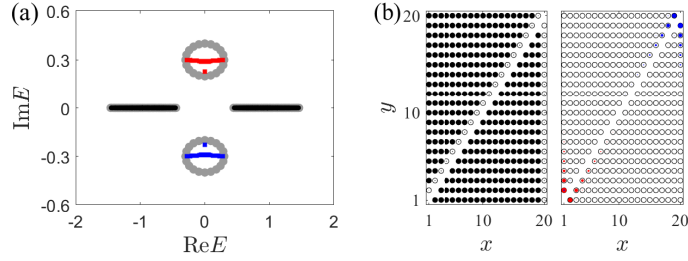


Figure S4. (color online). **Geometry-independence of intrinsic hybrid skin-topological effect of  $H_{g,2D}$ .** (a) Energy spectrum for Hamiltonian  $H_{g,2D}$  in Eq.(5) of the main text under triangle geometry. Black circles correspond to bulk states and red (blue) squares correspond to boundary states with positive (negative) imaginary energies. Gray circles show  $x$ -OBC/ $y$ -PBC spectra for the same Hamiltonian. (b) Spatial distribution of states under triangle geometry, marked by the same colors as in (a). Parameters are  $u = 0.2$ ,  $v = 1$ ,  $g = 0.3$ ,  $t_1 = 0.3$  and  $t'_2 = 0.1$  for all panels.

## V. GEOMETRY-INDEPENDENCE OF THE INTRINSIC HYBRID SKIN-TOPOLOGICAL EFFECTS

In this section, we discuss the intrinsic hybrid skin-topological effect of  $H_{g,2D}$  in Eq.(5) of the main text with different geometries. As shown in Fig. 3(a) of the main text, the bulk spectrum of  $H_{g,2D}$  is given by 1D lines and covers zero area in the complex plane. As discussed in Ref. [62], this property reveals that the absence of bulk NHSE is independent from the system's geometry, hence we denote it as the intrinsic hybrid skin-topological effect. To verify this, we demonstrate the complex spectrum and spatial distribution of eigenstates of Hamiltonian  $H_{g,2D}$  under triangle geometry in Fig. S4. As seen in Fig. S4(a), the bulk spectrum (black) is still consistent with the  $x$ -OBC/ $y$ -PBC spectrum (gray). And as further demonstrated in Fig. S4(b), bulk states are extended in the triangle lattice and are free from NHSE, while edge states suffer from NHSE and are located at corners.

In contrast, we can construct another Hamiltonian as followed,

$$H_{g,2D}^{(\text{geo})} = H_g + t'_2 \cos k_y \sigma_z + it_1 \sin k_y \sigma_0, \quad (\text{S15})$$

which is similar to Hamiltonian  $H_{g,2D}$  but with an extra  $\pi$  phase to the hopping toward positive  $y$  direction. This Hamiltonian also supports hybrid skin-topological effect under square geometry, as demonstrated in Fig. S5 (a) and S5 (b). However, its bulk spectrum covers a non-vanishing area in the complex plane, suggesting the emergence of bulk NHSE on certain geometries. Specifically, we find that the bulk states suffer from NHSE under triangle geometry, localizing along the hypotenuse of the triangle, as demonstrated in Fig. S5 (c) and (d).

## VI. EFFECTIVE SURFACE HAMILTONIAN FOR 3D GENERALIZATIONS

In this section, we provide the effective surface Hamiltonian of the 3D system discussed in the main text.

The Hamiltonians  $H_{\gamma/g,3D}$  and  $H'_{g,3D}$  in the main text are chosen to support surface states on (001) and (00 $\bar{1}$ ) surfaces. Corresponding projectors of these surface states are

$$\hat{P}_{\pm,3D} = (1 \pm \sigma_0 \tau_z)/2.$$

Thereby, the effective surface Hamiltonian of  $H_{\gamma,3D}$  can be given by:

$$\begin{aligned} H_{\gamma,\text{surf}}^{\pm} &= \hat{P}_{\pm,3D} H_{\gamma,3D} \hat{P}_{\pm,3D} \\ &= \pm i \{ t_1 \cos k_y \sigma_0 + (u + v \cos k_x) \sigma_x + [v \sin k_x \pm i(\gamma/2 + t_2 \sin k_y)] \sigma_y \}. \end{aligned} \quad (\text{S16})$$

Comparing to Eq.(1) of the main text, we find the effective Hamiltonian  $H_{\gamma,\text{surf}}^{\pm}$  can be considered as  $\pm i H_{\gamma,2D}$  (the signs of  $\gamma$  and  $t_2$  are flipped for  $H_{\gamma,\text{surf}}^-$ ). As discussed in Sec II,  $H_{\gamma,2D}$  holds a non-Bloch  $\mathcal{PT}$  symmetry. Correspondingly,  $H_{\gamma,\text{surf}}^{\pm}$  holds a non-Bloch  $\mathcal{CP}$  symmetry, due to the additional imaginary factor  $\pm i$ . Therefore, the surface states of  $H_{\gamma,3D}$  can support various NHSE channels activated by  $\mathcal{CP}$  symmetry breaking, as discussed in the main text with Fig. 4(a) to (c).

Similarly, the effective surface Hamiltonian of  $H_{g,3D}$  reads

$$H_{g,\text{surf}}^{\pm} = \hat{P}_{\pm,3D} H_{g,3D} \hat{P}_{\pm,3D} = \pm i H_{g,2D}. \quad (\text{S17})$$

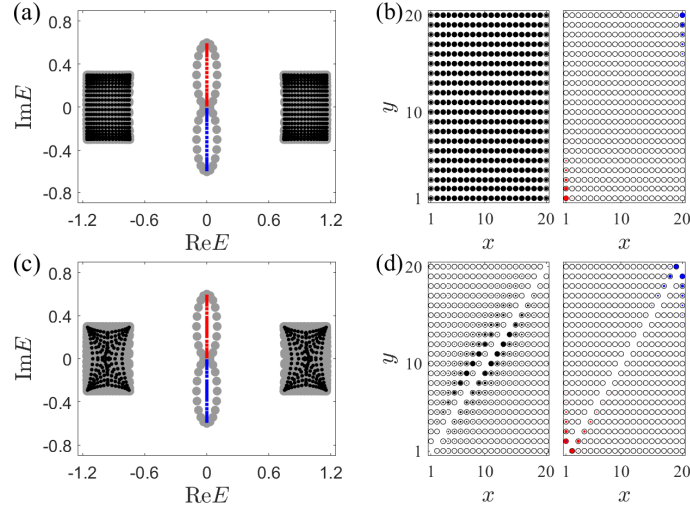


Figure S5. (color online). **Geometry-dependence of conventional hybrid skin-topological effect of  $H_{g,2D}^{(geo)}$ .** (a) Energy spectrum of Hamiltonian  $H_{g,2D}^{(geo)}$  in Eq. (S15) under square geometry. Black circles corresponds to bulk states and red (blue) squares corresponds to boundary states with positive (negative) imaginary energies. Gray circles shows  $x$ -OBC/ $y$ -PBC spectrum for the same Hamiltonian. (b) Spatial distribution for states under square geometry, marked by the same colors as in (a). (c) and (d) the same as (a) and (b), but under triangle geometry. Parameters are  $u = 0.2$ ,  $v = 1$ ,  $g = 0.3$ ,  $t_1 = 0.3$  and  $t_2' = 0.1$  for all panels.

Therefore,  $H_{g,\text{surf}}^\pm$  satisfies a  $\mathcal{CP}$  symmetry  $[\mathcal{CP}, H_{g,\text{surf}}^\pm]_+ = 0$  with  $\mathcal{CP} = \sigma_x \mathcal{K}$ . And the surface (hinge) states of  $H_{g,3D}$  displays similar NHSE phenomenon as the bulk (and edge) states of  $H_{g,2D}$ , as shown in Fig.4(d) of the main text.

The effective surface Hamiltonian of  $H'_{g,3D}$  is given by

$$H_{g,\text{surf}}^{\pm'} = \hat{P}_{\pm,3D} H'_{g,3D} \hat{P}_{\pm,3D} = \pm i [H_{g,2D} \mp i(t_2' \sin k_y + g)\sigma_0], \quad (\text{S18})$$

where the  $\mathcal{CP}$  symmetry is broken and then surface states suffer from NHSE. However, one branch of boundary states of  $H_{g,\text{surf}}^{\pm'}$  recovers  $\mathcal{CP}$  symmetry and is free from NHSE, analogous with the discussion of  $H'_{g,2D}$  in the main text. In this 3D model,  $\mathcal{CP}$  symmetry is recover for distinct branches of boundary states in the (001) and (00 $\bar{1}$ ) surfaces because of the  $\mp$  sign in the square bracket of the Eq.(S18). As a result, these NHSE-free hinge states living in these two surfaces are localized in opposite sides along  $x$ -direction, as shown in Fig.4(e) (green) in the main text.

Finally, the projectors of (001) and (00 $\bar{1}$ ) surface states for the Hamiltonian  $H'_{3D}$  in the main text are

$$\hat{P}'_{\pm,3D} = (1 \pm \sigma_z \tau_0)/2.$$

Their effective surface Hamiltonian can be obtained as

$$\begin{aligned} H_{3D,\text{surf}}^{\pm'} &= \hat{P}'_{\pm,3D} H'_{3D} \hat{P}'_{\pm,3D} \\ &= t_1 \cos k_y \tau_0 \pm [(u' + v' \cos k_x)\tau_x + v' \sin k_x \tau_y], \end{aligned} \quad (\text{S19})$$

which satisfies a  $\mathcal{PT}$  symmetry  $[\mathcal{PT}, H_{3D,\text{surf}}^{\pm'}] = 0$  with  $\mathcal{PT} = \tau_x \mathcal{K}$ . Actually,  $H_{3D,\text{surf}}^{\pm'}$  is Hermitian and without NHSE. Correspondingly, the dimensionality of surface and hinge states of  $H'_{3D}$  is unchanged by NHSE, despite that the localizing direction of hinge states (green) are altered by the  $z$ -NHSE, as shown in Figs.4(f) and 4(g) of the main text. Meanwhile, the bulk states can show distinct localization with various types of NHSE, as shown in Figs.4(f) and 4(g) of the main text.

[1] C. M. Bender and S. Boettcher, Phys. Rev. Lett. **80**, 5243 (1998).

[2] C. M. Bender, Rep. Prog. Phys. **70**, 947 (2007).

[3] E. J. Bergholtz, J. C. Budich, and F. K. Kunst, Rev.

- Mod. Phys. **93**, 015005 (2021).
- [4] A. Mostafazadeh, Journal of Mathematical Physics **43**, 205 (2002).
  - [5] R. El-Ganainy, K. G. Makris, M. Khajavikhan, Z. H. Musslimani, S. Rotter, and D. N. Christodoulides, Nat. Phys. **14**, 11 (2018).
  - [6] L. Feng, R. El-Ganainy, and L. Ge, Nature Photonics **11**, 752 (2017).
  - [7] A. Regensburger, C. Bersch, M.-A. Miri, G. Onishchukov, D. N. Christodoulides, and U. Peschel, Nature **488**, 167 (2012).
  - [8] H. Zhao and L. Feng, National Science Review **5**, 183 (2018).
  - [9] Ş. K. Özdemir, S. Rotter, F. Nori, and L. Yang, Nature materials **18**, 783 (2019).
  - [10] X. Zhu, H. Ramezani, C. Shi, J. Zhu, and X. Zhang, Physical Review X **4**, 031042 (2014).
  - [11] R. Fleury, D. Sounas, and A. Alù, Nature communications **6**, 1 (2015).
  - [12] C. Shi, M. Dubois, Y. Chen, L. Cheng, H. Ramezani, Y. Wang, and X. Zhang, Nature communications **7**, 1 (2016).
  - [13] L. Shao, W. Mao, S. Maity, N. Sinclair, Y. Hu, L. Yang, and M. Lončar, Nature Electronics **3**, 267 (2020).
  - [14] Y. Choi, C. Hahn, J. W. Yoon, and S. H. Song, Nature communications **9**, 2182 (2018).
  - [15] T. Wang, J. Fang, Z. Xie, N. Dong, Y. N. Joglekar, Z. Wang, J. Li, and L. Luo, The European Physical Journal D **74**, 1 (2020).
  - [16] A. Stegmaier, S. Imhof, T. Helbig, T. Hofmann, C. H. Lee, M. Kremer, A. Fritzsche, T. Feichtner, S. Klemmt, S. Höfling, *et al.*, Physical Review Letters **126**, 215302 (2021).
  - [17] C. Hang, G. Huang, and V. V. Konotop, Physical review letters **110**, 083604 (2013).
  - [18] Z. Zhang, Y. Zhang, J. Sheng, L. Yang, M.-A. Miri, D. N. Christodoulides, B. He, Y. Zhang, and M. Xiao, Physical review letters **117**, 123601 (2016).
  - [19] P. Peng, W. Cao, C. Shen, W. Qu, J. Wen, L. Jiang, and Y. Xiao, Nature Physics **12**, 1139 (2016).
  - [20] A. K. Jahromi, A. U. Hassan, D. N. Christodoulides, and A. F. Abouraddy, Nature communications **8**, 1359 (2017).
  - [21] J. Li, A. K. Harter, J. Liu, L. de Melo, Y. N. Joglekar, and L. Luo, Nat. Comm. **10**, 855 (2019).
  - [22] A. L. Muniz, M. Wimmer, A. Bisianov, U. Peschel, R. Morandotti, P. S. Jung, and D. N. Christodoulides, Physical Review Letters **123**, 253903 (2019).
  - [23] R. Lin, T. Tai, L. Li, and C. H. Lee, arXiv preprint arXiv:2302.03057 (2023).
  - [24] X. Zhang, T. Zhang, M.-H. Lu, and Y.-F. Chen, Advances in Physics: X **7**, 2109431 (2022).
  - [25] S. Yao, F. Song, and Z. Wang, Phys. Rev. Lett. **121**, 136802 (2018).
  - [26] F. Song, S. Yao, and Z. Wang, Physical review letters **123**, 246801 (2019).
  - [27] F. Song, S. Yao, and Z. Wang, Physical review letters **123**, 170401 (2019).
  - [28] L. Li, C. H. Lee, and J. Gong, Physical Review B **100**, 075403 (2019).
  - [29] H. Jiang, L.-J. Lang, C. Yang, S.-L. Zhu, and S. Chen, Physical Review B **100**, 054301 (2019).
  - [30] S. Longhi, Physical Review Letters **122**, 237601 (2019).
  - [31] Q.-B. Zeng, Y.-B. Yang, and Y. Xu, Physical Review B **101**, 020201 (2020).
  - [32] K. Yokomizo and S. Murakami, Physical review letters **123**, 066404 (2019).
  - [33] C. Lee and R. Thomale, Phys. Rev. B **99**, 201103(R) (2019).
  - [34] Z. Yang, K. Zhang, C. Fang, and J. Hu, Physical Review Letters **125**, 226402 (2020).
  - [35] L. Li, C. H. Lee, S. Mu, and J. Gong, Nature communications **11**, 5491 (2020).
  - [36] Y. Yi and Z. Yang, Phys. Rev. Lett. **125**, 186802 (2020).
  - [37] C. H. Lee, Physical Review B **104**, 195102 (2021).
  - [38] M. Lu, X.-X. Zhang, and M. Franz, Phys. Rev. Lett. **127**, 256402 (2021).
  - [39] D. S. Borgnia, A. J. Kruchkov, and R.-J. Slager, Phys. Rev. Lett. **124**, 056802 (2020).
  - [40] K. Zhang, Z. Yang, and C. Fang, Phys. Rev. Lett. **125**, 126402 (2020).
  - [41] N. Okuma, K. Kawabata, K. Shiozaki, and M. Sato, Phys. Rev. Lett. **124**, 086801 (2020).
  - [42] L. Li, C. H. Lee, and J. Gong, Communications Physics **4**, 42 (2021).
  - [43] C.-X. Guo, C.-H. Liu, X.-M. Zhao, Y. Liu, and S. Chen, Phys. Rev. Lett. **127**, 116801 (2021).
  - [44] L. Li, S. Mu, C. H. Lee, and J. Gong, Nature communications **12**, 5294 (2021).
  - [45] Y. Liu, Y. Wang, X.-J. Liu, Q. Zhou, and S. Chen, Phys. Rev. B **103**, 014203 (2021).
  - [46] Y. Liu, Y. Zeng, L. Li, and S. Chen, Phys. Rev. B **104**, 085401 (2021).
  - [47] T. Li, Y.-S. Zhang, and W. Yi, Chinese Physics Letters **38**, 030301 (2021).
  - [48] P.-C. Cao, Y.-G. Peng, Y. Li, and X.-F. Zhu, Chinese Physics Letters **39**, 057801 (2022).
  - [49] R. Shen and C. H. Lee, Communications Physics **5**, 238 (2022).
  - [50] S. Longhi, Phys. Rev. Lett. **128**, 157601 (2022).
  - [51] X.-Q. Sun, P. Zhu, and T. L. Hughes, Phys. Rev. Lett. **127**, 066401 (2021).
  - [52] B. A. Bhargava, I. C. Fulga, J. van den Brink, and A. G. Moghaddam, Phys. Rev. B **104**, L241402 (2021).
  - [53] F. Schindler and A. Prem, Phys. Rev. B **104**, L161106 (2021).
  - [54] A. Panigrahi, R. Moessner, and B. Roy, Phys. Rev. B **106**, L041302 (2022).
  - [55] C. H. Lee, L. Li, and J. Gong, Phys. Rev. Lett. **123**, 016805 (2019).
  - [56] L. Li, C. H. Lee, and J. Gong, Phys. Rev. Lett. **124**, 250402 (2020).
  - [57] Y. Li, C. Liang, C. Wang, C. Lu, and Y.-C. Liu, Phys. Rev. Lett. **128**, 223903 (2022).
  - [58] T. Tai and C. H. Lee, arXiv preprint arXiv:2202.03462 (2022).
  - [59] R. Yang, J. W. Tan, T. Tai, J. M. Koh, L. Li, S. Longhi, and C. H. Lee, Science Bulletin **67**, 1865 (2022).
  - [60] W. Zhu and J. Gong, arXiv preprint arXiv:2203.03284 (2022).
  - [61] F. Qin, Y. Ma, R. Shen, and C. H. Lee, arXiv preprint arXiv:2212.13536 (2022).
  - [62] K. Zhang, Z. Yang, and C. Fang, Nat. Commun. **13**, 2496 (2022).
  - [63] Y. Qin, K. Zhang, and L. Li, 2304.03792v1.
  - [64] L. Li and C. H. Lee, Science Bulletin **67**, 685 (2022).
  - [65] H. Jiang and C. H. Lee, 2207.08843v2.

- [66] W. Wang, X. Wang, and G. Ma, *Phys. Rev. Lett.* **129**, 264301 (2022).
- [67] D. Zou, T. Chen, W. He, J. Bao, C. H. Lee, H. Sun, and X. Zhang, *Nat. Commun.* **12**, 7201 (2021).
- [68] Z. Ou, Y. Wang, and L. Li, *Phys. Rev. B* **107**, L161404 (2023).
- [69] H. Zhang, T. Chen, L. Li, C. H. Lee, and X. Zhang, *Phys. Rev. B* **107**, 085426 (2023).
- [70] I. Petrides, H. M. Price, and O. Zilberberg, *Physical Review B* **98**, 125431 (2018).
- [71] C. H. Lee, Y. Wang, Y. Chen, and X. Zhang, *Physical Review B* **98**, 094434 (2018).
- [72] X. Zhang, G. Li, Y. Liu, T. Tai, R. Thomale, and C. H. Lee, *Communications Physics* **4**, 47 (2021).
- [73] R. Okugawa, R. Takahashi, and K. Yokomizo, *Physical Review B* **102**, 241202 (2020).
- [74] W. A. Benalcazar, B. A. Bernevig, and T. L. Hughes, *Science* **357**, 61 (2017).
- [75] W. A. Benalcazar, B. A. Bernevig, and T. L. Hughes, *Phys. Rev. B* **96**, 245115 (2017).
- [76] Y. Langbehn, J. Peng, L. Trifunovic, F. von Oppen, and P. W. Brouwer, *Phys. Rev. Lett.* **119**, 246401 (2017).
- [77] Z. Song, Z. Fang, and C. Fang, *Phys. Rev. Lett.* **119**, 246402 (2017).
- [78] W. P. Su, J. R. Schrieffer, and A. J. Heeger, *Phys. Rev. B* **22**, 2099 (1980).
- [79] T. E. Lee, *Phys. Rev. Lett.* **116**, 133903 (2016).
- [80] S. Yao and Z. Wang, *Phys. Rev. Lett.* **121**, 086803 (2018).
- [81] F. K. Kunst, E. Edvardsson, J. C. Budich, and E. J. Bergholtz, *Phys. Rev. Lett.* **121**, 026808 (2018).
- [82] C. Yin, H. Jiang, L. Li, R. Lü, and S. Chen, *Phys. Rev. A* **97**, 052115 (2018).
- [83] S. Lieu, *Phys. Rev. B* **97**, 045106 (2018).
- [84] Supplemental Materials.
- [85] S. Longhi, *Phys. Rev. Res.* **1**, 023013 (2019).
- [86] L. Xiao, T. Deng, K. Wang, Z. Wang, W. Yi, and P. Xue, *Physical Review Letters* **126**, 230402 (2021).
- [87] M. Geier, L. Trifunovic, M. Hoskam, and P. W. Brouwer, *Phys. Rev. B* **97**, 205135 (2018).
- [88] L. Trifunovic and P. W. Brouwer, *Phys. Rev. X* **9**, 011012 (2019).
- [89] Z. Lei, Y. Deng, and L. Li, *Phys. Rev. B* **106**, 245105 (2022).
- [90] Z. Lei, L. Li, and Y. Deng, *Phys. Rev. B* **107**, 115166 (2023).
- [91] Z. Gong, Y. Ashida, K. Kawabata, K. Takasan, S. Higashikawa, and M. Ueda, *Phys. Rev. X* **8**, 031079 (2018).
- [92] L. Xiao, T. Deng, K. Wang, G. Zhu, Z. Wang, W. Yi, and P. Xue, *Nature Physics* **16**, 761 (2020).
- [93] Q. Lin, T. Li, L. Xiao, K. Wang, W. Yi, and P. Xue, *Nature Communications* **13**, 3229 (2022).
- [94] L. Xiao, W.-T. Xue, F. Song, Y.-M. Hu, W. Yi, Z. Wang, and P. Xue, *arXiv preprint arXiv:2303.12831* (2023).
- [95] J. Wang, S. Valligatla, Y. Yin, L. Schwarz, M. Medina-Sánchez, S. Baunack, C. H. Lee, R. Thomale, S. Li, V. M. Fomin, *et al.*, *Nature Photonics* **17**, 120 (2023).
- [96] Q. Liang, D. Xie, Z. Dong, H. Li, H. Li, B. Gadway, W. Yi, and B. Yan, *Phys. Rev. Lett.* **129**, 070401 (2022).
- [97] A. J. Kollár, M. Fitzpatrick, and A. A. Houck, *Nature* **571**, 45 (2019).
- [98] A. Smith, M. Kim, F. Pollmann, and J. Knolle, *npj Quantum Information* **5**, 106 (2019).
- [99] L. Bassman, M. Urbanek, M. Metcalf, J. Carter, A. F. Kemper, and W. A. de Jong, *Quantum Science and Technology* **6**, 043002 (2021).
- [100] M. Ippoliti, K. Kechedzhi, R. Moessner, S. Sondhi, and V. Khemani, *PRX Quantum* **2**, 030346 (2021).
- [101] J. M. Koh, T. Tai, Y. H. Phee, W. E. Ng, and C. H. Lee, *npj Quantum Information* **8**, 16 (2022).
- [102] J. M. Koh, T. Tai, and C. H. Lee, *Physical Review Letters* **129**, 140502 (2022).
- [103] X. Zhang, W. Jiang, J. Deng, K. Wang, J. Chen, P. Zhang, W. Ren, H. Dong, S. Xu, Y. Gao, *et al.*, *Nature* **607**, 468 (2022).
- [104] J. M. Koh, T. Tai, and C. H. Lee, *arXiv preprint arXiv:2303.02179* (2023).
- [105] C. Fleckenstein, A. Zorzato, D. Varjas, E. J. Bergholtz, J. H. Bardarson, and A. Tiwari, *Physical Review Research* **4**, L032026 (2022).
- [106] P. Frey and S. Rachel, *Science Advances* **8**, eabm7652 (2022).
- [107] T. Chen, R. Shen, C. H. Lee, and B. Yang, *arXiv preprint arXiv:2210.13840* (2022).
- [108] T. Hofmann, T. Helbig, C. H. Lee, M. Greiter, and R. Thomale, *Physical review letters* **122**, 247702 (2019).
- [109] L. Li, C. H. Lee, and J. Gong, *Communications physics* **2**, 135 (2019).
- [110] T. Helbig, T. Hofmann, S. Imhof, M. Abdelghany, T. Kiessling, L. Molenkamp, C. Lee, A. Szameit, M. Greiter, and R. Thomale, *Nature Physics* **16**, 747 (2020).
- [111] C. Shang, S. Liu, R. Shao, P. Han, X. Zang, X. Zhang, K. N. Salama, W. Gao, C. H. Lee, R. Thomale, *et al.*, *Advanced Science* **9**, 2202922 (2022).
- [112] J. Wu, X. Huang, Y. Yang, W. Deng, J. Lu, W. Deng, and Z. Liu, *Physical Review B* **105**, 195127 (2022).
- [113] P. M. Lenggenhager, A. Stegmaier, L. K. Upreti, T. Hofmann, T. Helbig, A. Vollhardt, M. Greiter, C. H. Lee, S. Imhof, H. Brand, *et al.*, *Nature Communications* **13**, 4373 (2022).
- [114] P. Zhu, X.-Q. Sun, T. L. Hughes, and G. Bahl, *Nature communications* **14**, 720 (2023).
- [115] S. Longhi, *Optics Letters* **44**, 5804 (2019).
- [116] W. Zhu, W. X. Teo, L. Li, and J. Gong, *Phys. Rev. B* **103**, 195414 (2021).